PCCP

PAPER

View Article Online
View Journal | View Issue

Cite this: *Phys. Chem. Chem. Phys.*, 2025, **27**, 5087

First-principle oligopeptide structural optimization with physical prior mean-driven Gaussian processes: a test of synergistic impacts of the kernel functional and coordinate system†

Yibo Chang, Chong Teng and Junwei Lucas Bao *

First-principle molecular structural determination is critical in many aspects of computational modeling, and yet, the precise determination of a local minimum for a large-sized organic molecule is time-consuming. The recently developed nonparametric model, the physical Gaussian Processes (GPs) with physics-informed prior mean function, has demonstrated its efficiency in exploring the potential-energy surfaces and molecular geometry optimizations. Two essential ingredients in physical GPs, the kernel functional and the coordinate systems, could impact the optimization efficiency, and yet the choice of which on the model performance has not yet been studied. In this work, we constructed a testing dataset consisting of 20 oligopeptides and performed a systematic investigation using various combinations of coordinates (structural descriptors) and kernel functionals to optimize these biologically interesting molecules to local minima at the density-functional tight-binding (DFTB) quantum mechanical level. We conclude that the combination of the kernel functional form and coordinate systems matter significantly in model performance as well as its robustness in locating local minima. For our testing set, the synergy between the periodic kernel and the non-redundant delocalized internal coordinates yields the best overall performance for physical GPs, significantly superior to other choices.

Received 17th November 2024,
Accepted 12th February 2025

DOI: 10.1039/d4cp04378b

rsc.li/pccp

I. Introduction

Molecular structural optimization is one of the cornerstones in computational modeling of chemistry, materials, and chemical biology. One starts with a set of initial-guess structures, in which the atomic coordinates are built based on chemical knowledge, known bond lengths or angles, and the atomic hybridization states, and this set of initial structures undergoes geometry optimization to relax their electronic structure energies to reach local minima. In the case of finding a transition-state structure, the initial structure is relaxed to a first-order saddle point that connects the reactant with the product's local minimum structures. The energies and gradients at a non-stationary structure are commonly generated by quantum chemistry calculations on the fly, which are used to guide the search directions. This task of determining molecular structure is equivalent to a multidimensional optimization problem in computational science. In particular, the target function, $E(\boldsymbol{x})$, is a function of all atomic coordinates, $\boldsymbol{x}$, in the molecule. The local minimum on this potential energy surface (PES) corresponds to a structure of chemical interest.

For small molecules, the computational cost associated with structural optimizations is manageable. Nevertheless, since the dimensionality quickly grows as the molecule becomes larger, the optimization itself becomes costly, in addition to the cost of computing energies and gradients. Therefore, biologically interesting small molecules, which are often too large from the perspective of molecular chemistry, are usually treated at a lower level of theory. One either does not optimize the structure to a local minimum and relies on dynamic sampling or docking to qualitatively explore the structural information, or one optimizes the structure with classical mechanics, *i.e.*, classical force fields, to gain qualitative insights on structural features. Both approaches are indeed effective, especially when experimentally resolved structural information for similar systems is available for comparison. Nevertheless, due to the intrinsic limit and uncertainty in these methods, *e.g.*, the inability of classical force fields to describe electron correlation-induced non-covalent interactions with high accuracy (or the interaction parameters for the system under study are missing), a fully

Department of Chemistry, Boston College, Chestnut Hill, Massachusetts 02467, USA. E-mail: lucas.bao@bc.edu

† Electronic supplementary information (ESI) available. See DOI: https://doi.org/10.1039/d4cp04378b

quantum mechanical (QM) structural optimization may be preferred. To be more specific, if affordable, a first-principle determination (without system-dependent parameters) with a quantitatively reliable energy calculation would be beneficial to predicting structures at a higher resolution. Density-functional theory (DFT),[1,2] including its semi-empirical approximation, the density-functional tight-binding (DFTB) theory,[3–13] provides an excellent balance between computational cost and accuracy, in this context, for main-group chemistry and molecules. Although models like AlphaFold[14–17] provide sophisticated direct predictions of dominant conformations for macromolecules such as proteins without relying on first-principles calculations or conventional geometry optimization, the relatively small and conformationally flexible oligopeptides and polypeptides are underrepresented in their training data. Consequently, first-principles structural determination, including the exploration of the entire ensemble of conformers accessible at around room temperature, remains critical. This approach not only complements predictive models like AlphaFold but is also crucial for achieving high-accuracy quantum chemistry modeling. Our work addresses this need by studying a new method to accelerate oligopeptide structure optimizations, enhancing the accuracy and efficiency of first-principles calculations for these challenging systems.

Even with computationally efficient quantum chemistry methods for calculating energies and forces, the optimization itself remains a computational bottleneck for higher-dimensional systems, such as polypeptides, macrocyclic peptides, and oligopeptides, which are important in biological chemistry and therapeutics. Structural predictions continue to attract the efforts of practitioners, including the application of advanced reinforcement machine learning techniques for small molecular geometry optimizations.[18] We have recently developed an on-the-fly learning model, the physical prior mean-driven Gaussian Processes (GPs),[19] to mitigate the high computational cost associated with geometry optimizations. A GP with a constant prior mean does not include prior physical approximation to the PES; nevertheless, such a model is still useful in local minimum search[20–23] and PES exploration,[24–28] albeit its efficiency and robustness could be further enhanced due to the criticalness of physicochemical information in structure search.[29] GPs are a class of nonparametric models rooted in Bayesian probability, exploring functional space with a prior mean that characterizes the assumed probabilistic distribution *a priori*.[30] In our model, the prior mean is chosen based on a lower-order approximation to the true PES, *e.g.*, a simple classical force field,[19] a semi-empirical molecular orbital theory, an adaptive set of computationally efficient models,[31,32] or a previously learned PES.[33] Without the need to pre-constructing an extensive dataset for training the PES to be explored, one directly starts the geometry optimization task on the GPs' surrogate PES (SPES), and the surrogate posterior mean learns from the QM information (energies and gradients) on the fly and drives the optimizer to reach a local minimum, completing the GP-assisted *ab initio* molecular structure determination. This critical feature makes the model highly data-efficient and permits real-time learning and predictions.

Although nonparametric, the model performance of physical GPs is determined by three components primarily: the kernel functional, coordinate systems, and the physical prior mean function. We have previously studied the benefit of introducing physical prior mean function, which not only makes the model robust and efficient but, more importantly, the learned surrogate closely resembles the ground truth (true full QM PES) even for the underexplored region, permitting its future recycling in other tasks as well as meta-learning. The kernel functional $k(\boldsymbol{x}_i,\boldsymbol{x}_j)$ is fundamental in GPs because it defines how the points ($\boldsymbol{x}_i$ and $\boldsymbol{x}_j$) in the input space are covariant with one another, impacting the optimizer's robustness and generalization ability,[34] and influencing the smoothness of the SPESs. When combined with molecular structural descriptors, namely, coordinate representation of the structure ($\boldsymbol{x}_i$, which is itself a function of atomic Cartesian coordinates), the kernel functional encodes physical knowledge *a priori* as well, controlling the model flexibility, complexity, and how sensitive it responds to the correlation between two structures on the same QM PES. We expect such an impact would become much more evident for molecules with more than 100 atoms, the optimization costs of which are no longer negligible. Given the unique importance of the definition of $k(\boldsymbol{x}_i,\boldsymbol{x}_j)$, which includes the choice of the functional form of k and the structural descriptor $\boldsymbol{x}$, in this work, we present a systematic study to explore how the efficiency of our physical GP optimizer is impacted by it for large-sized molecules, in particular, first-principle oligopeptide structural optimization.

We constructed a testing dataset consisting of 20 oligopeptides and implemented four commonly used kernels (including the squared exponential kernel, the twice differentiable Matern kernel, the rational quadratic kernel, and the periodic kernel) combined with three types of internal coordinates frequently used in computational chemistry (including the redundant internal coordinates, non-redundant internal coordinates, and the Coulombic coordinates). Note that it is well-known that atomic Cartesian coordinates themselves are not good coordinate choices for molecular geometry optimizations, even for small molecules, due to numerical inefficiency, breakdown of PES invariance to overall translation and rotation, and potentially unphysical changes in bond lengths and angles. Consequently, we did not test the optimization performance in Cartesian coordinates in this work.

II. Theory background overview

Gaussian processes (GPs) with physical prior mean

In physical GPs, the surrogate (SPES) is constructed as a weighted average of the kernel, the derivatives of the kernel, and a non-constant physically inspired prior mean function, $\mu(\boldsymbol{x})$, as,

$$E^{\mathrm{SPES}}(\boldsymbol{x}) = \sum_{i=1}^{N}\left(k(\boldsymbol{x},\boldsymbol{x}_i)\alpha_i + \frac{\partial k(\boldsymbol{x},\boldsymbol{x}_i)}{\partial \boldsymbol{x}_i^{\mathrm{T}}}\boldsymbol{\beta}_i\right) + \mu(\boldsymbol{x}) \qquad (1)$$

where $\boldsymbol{x}$ is a molecular structure vector represented in a particular choice of the coordinate system, $k(\boldsymbol{x},\boldsymbol{x}_i)$ is a kernel functional that characterizes the structural similarity between the current structure $\boldsymbol{x}$ and a previous structure $\boldsymbol{x}_i$ included in the training using a Euclidean l^2-norm, $||\boldsymbol{x}-\boldsymbol{x}_i||$. The molecular structure descriptor $\boldsymbol{x}$ is a function of the atomic Cartesian coordinates. Note that the size of the GP training set, N, is adaptive on the fly, not determined *a priori*. The linear combination coefficients $\{\alpha_i\}$ and $\{\boldsymbol{\beta}_i\}$ are trained during the structural optimization. The above GP interpolation can be recast into the following linear systems,

$$\sum_{j=1}^{N}\left[\begin{pmatrix} k(\boldsymbol{x}_i,\boldsymbol{x}_j) & \dfrac{\partial k(\boldsymbol{x}_i,\boldsymbol{x}_j)}{\partial \boldsymbol{x}_j^{\mathrm{T}}} \\ \dfrac{\partial k(\boldsymbol{x}_i,\boldsymbol{x}_j)}{\partial \boldsymbol{x}_i} & \dfrac{\partial^2 k(\boldsymbol{x}_i,\boldsymbol{x}_j)}{\partial \boldsymbol{x}_i \partial \boldsymbol{x}_j^{\mathrm{T}}} \end{pmatrix} + \delta_{ij}\begin{pmatrix} {\sigma_{\mathrm{e}}}^2 & \mathbf{0} \\ \mathbf{0} & {\sigma_{\mathrm{f}}}^2\mathbf{I} \end{pmatrix}\right]\begin{pmatrix} \alpha_j \\ \boldsymbol{\beta}_j \end{pmatrix} = \begin{pmatrix} E_i \\ -\boldsymbol{F}_i \end{pmatrix} - \begin{pmatrix} \mu(\boldsymbol{x}_i) \\ \nabla_{\boldsymbol{x}_i}\mu(\boldsymbol{x}_i) \end{pmatrix} \tag{2}$$

where E_i and $-\boldsymbol{F}_i$ are the energy and negative force (*i.e.*, $-\boldsymbol{F}_i = \boldsymbol{\nabla}_{\boldsymbol{x}}E^{\mathrm{SPES}}(\boldsymbol{x})$) of the structure x_i. $\mathbf{I}$ is the identity matrix, δ_{ij} is the Kronecker delta. The noise parameters for energy (${\sigma_{\mathrm{e}}}^2$ in eV) and force (${\sigma_{\mathrm{f}}}^2$ in eV Å^{-1}) are implemented in GP training to improve the numerical stability and avoid overfitting the numerical noises, namely, the insignificant numerals below the self-consistent field (SCF) convergence threshold and the corresponding accuracy in the calculated force. The nth-order kernel derivatives can be evaluated analytically using techniques in matrix and tensor differentiation[35,36] or by the automatic differentiation (AD) method.[37]

Kernel functional

The kernel functional defines the reproducing kernel Hilbert space according to Mercer's theorem, and consequently, the functional space that GPs search and the posterior sample path (*i.e.*, when we condition the GP on the QM energies and forces, a single function drawn from the GP's distribution), influencing the posterior mean prediction (*i.e.*, the SPES). In this work, we implemented the following four kernel functionals to explore their efficiency and effectiveness in GP optimization of large-sized molecules.

(A) The squared exponential (SE) kernel (also known as the radial basis function (RBF) kernel):

$$k^{\mathrm{SE}}(\boldsymbol{x}_i,\boldsymbol{x}_j) = \exp\left[-\frac{\left(\|\boldsymbol{x}_i-\boldsymbol{x}_j\|\right)^2}{2l^2}\right] \tag{3}$$

in which l is a scalar length scale hyperparameter, which is set to a generic value (refer to the Computational Details section) without *ad hoc* tuning. k^{SE} is infinitely differentiable, permitting GP to search in a space consisting of very smooth functions. Its first-order derivative is,

$$\frac{\partial k^{\mathrm{SE}}(\boldsymbol{x}_i,\boldsymbol{x}_j)}{\partial \boldsymbol{x}_i} = -\frac{k^{\mathrm{SE}}(\boldsymbol{x}_i,\boldsymbol{x}_j)}{l^2}\cdot(\boldsymbol{x}_i-\boldsymbol{x}_j) \tag{4}$$

In addition, the first-order derivative is anti-symmetric, meaning that $\partial k^{\mathrm{SE}}/\partial \boldsymbol{x}_i = -\partial k^{\mathrm{SE}}/\partial \boldsymbol{x}_j$. Its second-order derivative is,

$$\frac{\partial^2 k^{\mathrm{SE}}(\boldsymbol{x}_i,\boldsymbol{x}_j)}{\partial \boldsymbol{x}_i \partial \boldsymbol{x}_j^{\mathrm{T}}} = -\frac{k^{\mathrm{SE}}(\boldsymbol{x}_i,\boldsymbol{x}_j)}{l^2}\left[\frac{(\boldsymbol{x}_i-\boldsymbol{x}_j)\otimes(\boldsymbol{x}_i-\boldsymbol{x}_j)}{l^2}-\mathbf{I}\right] \tag{5}$$

in which $\otimes$ is the outer product of two vectors, and $\mathbf{I}$ is the identity matrix.

(B) The rational quadratic (RQ) kernel:

$$k^{\mathrm{RQ}}(\boldsymbol{x}_i,\boldsymbol{x}_j) = \left[1+\frac{\left(\|\boldsymbol{x}_i-\boldsymbol{x}_j\|\right)^2}{2\alpha l^2}\right]^{-\alpha} \tag{6}$$

in which l is the length scale hyperparameter, and $\alpha > 0$ is the shape hyperparameter that controls the relative weighting of large-scale and small-scale variations. We set $\alpha = 1$ in this paper as a generic value because although the optimizer efficiency could be further tuned by changing this hyperparameter, it is impractical and inconvenient to do so in practical molecular geometry optimizations and predictions. Its first-order derivative is,

$$\frac{\partial k^{\mathrm{RQ}}(\boldsymbol{x}_i,\boldsymbol{x}_j)}{\partial \boldsymbol{x}_i} = -\frac{\left[k^{\mathrm{RQ}}(\boldsymbol{x}_i,\boldsymbol{x}_j)\right]^{1+1/\alpha}}{l^2}\cdot(\boldsymbol{x}_i-\boldsymbol{x}_j) \tag{7}$$

The RQ kernel is a generalization of the SE kernel, in particular, $\lim_{\alpha\to\infty} k^{\mathrm{RQ}} = k^{\mathrm{SE}}$. In addition, it can be viewed as an average of the SE kernels over a distribution of the inverse squared length scales, $l' = l^{-2}$, *i.e.*, $k^{\mathrm{RQ}} = \int_0^\infty k^{\mathrm{SE}}(\boldsymbol{x}_i,\boldsymbol{x}_j;l)p(l';\alpha)\mathrm{d}l'$, where $p(l';\alpha)$ is a gamma distribution of l'.[38] Compared to the SE kernel, which is more suitable for a uniform smoothness of data, the RQ kernel is flexible in describing the changes in smoothness in the input space, accommodating non-stationary regions on the PES, and capable of capturing its local and global patterns.

The second-order derivative of the RQ kernel is,

$$\frac{\partial^2 k^{\mathrm{RQ}}(\boldsymbol{x}_i,\boldsymbol{x}_j)}{\partial \boldsymbol{x}_i \partial \boldsymbol{x}_j^{\mathrm{T}}} = -\frac{1+\alpha}{\alpha l^4}\left[k^{\mathrm{RQ}}(\boldsymbol{x}_i,\boldsymbol{x}_j)\right]^{1+2/\alpha}(\boldsymbol{x}_i-\boldsymbol{x}_j)\otimes(\boldsymbol{x}_i-\boldsymbol{x}_j)+\frac{\left[k^{\mathrm{RQ}}(\boldsymbol{x}_i,\boldsymbol{x}_j)\right]^{1+1/\alpha}\mathbf{I}}{l^2} \tag{8}$$

(C) The twice differentiable Matern (M) kernel:

$$k^{\mathrm{M}}(\boldsymbol{x}_i,\boldsymbol{x}_j) = \left(1+\frac{\sqrt{5}\|\boldsymbol{x}_i-\boldsymbol{x}_j\|}{l}+\frac{5\left(\|\boldsymbol{x}_i-\boldsymbol{x}_j\|\right)^2}{3l^2}\right)\exp\left(-\frac{\sqrt{5}\|\boldsymbol{x}_i-\boldsymbol{x}_j\|}{l}\right) \tag{9}$$

Compared to the SE kernel, the twice differentiable Matern kernel provides moderate and finite degrees of smoothness. The SE kernel, on the other hand, is C^∞-differentiable and analytic at $\boldsymbol{x}_i = \boldsymbol{x}_j$, which may impose a too strong requirement for the underlying PES to be modeled. The twice differentiable

Matern kernel's first-order derivative is,

$$\frac{\partial k^{\mathrm{M}}(\boldsymbol{x}_i,\boldsymbol{x}_j)}{\partial \boldsymbol{x}_i}=-\frac{5}{3l^3}\left[\left(l+\sqrt{5}\|\boldsymbol{x}_i-\boldsymbol{x}_j\|\right)(\boldsymbol{x}_i-\boldsymbol{x}_j)\right]\exp\left(-\frac{\sqrt{5}\|\boldsymbol{x}_i-\boldsymbol{x}_j\|}{l}\right) \tag{10}$$

And, its second-order derivative is,

$$\frac{\partial^2 k^{\mathrm{M}}(\boldsymbol{x}_i,\boldsymbol{x}_j)}{\partial \boldsymbol{x}_i \partial \boldsymbol{x}_j^{\mathrm{T}}} = -\frac{5}{3l^3}\left[\frac{5}{l}(\boldsymbol{x}_i-\boldsymbol{x}_j)\otimes(\boldsymbol{x}_i-\boldsymbol{x}_j)-\left(l+\sqrt{5}\|\boldsymbol{x}_i-\boldsymbol{x}_j\|\right)\mathbf{I}\right] \times \exp\left(-\frac{\sqrt{5}\|\boldsymbol{x}_i-\boldsymbol{x}_j\|}{l}\right) \tag{11}$$

(D) The periodic (P) kernel:

$$k^{\mathrm{P}}(\boldsymbol{x}_i,\boldsymbol{x}_j)=\exp\left[-\frac{2\sin^2(\pi\|\boldsymbol{x}_i-\boldsymbol{x}_j\|/p)}{l^2}\right] \tag{12}$$

where the periodicity hyperparameter is chosen to be a generic value, $p = 2\pi$, in this work. We consider this kernel interesting because there are multiple torsional degrees of freedom in oligopeptide or large chain-shape molecules in general, and each torsional motion corresponds to a dihedral angle variation (from 0 to 2π) in the projected torsional PES, which usually resembles periodic characters due to the existence of multiple (nearly) identical local minima and torsional transition-state structures. Although torsional motions are coupled in a molecule, the concept of a local periodicity averaged over all internal rotations is still applicable and effective in treating torsional anharmonicity.[39–43] The first-order derivative of the periodic kernel is,

$$\frac{\partial k^{\mathrm{P}}(\boldsymbol{x}_i,\boldsymbol{x}_j)}{\partial \boldsymbol{x}_i}=-\frac{2\pi}{l^2 p}\sin\left(2\pi\|\boldsymbol{x}_i-\boldsymbol{x}_j\|/p\right)\cdot k^{\mathrm{P}}(\boldsymbol{x}_i,\boldsymbol{x}_j)\cdot \boldsymbol{e}_{ij} = g(d_{ij})\cdot \boldsymbol{e}_{ij} \tag{13}$$

where the unit vector $\boldsymbol{e}_{ij} = (\boldsymbol{x}_i - \boldsymbol{x}_j)/||\boldsymbol{x}_i - \boldsymbol{x}_j||$, and the scalar Euclidean distance $d_{ij} = ||\boldsymbol{x}_i - \boldsymbol{x}_j||$.

Its second-order derivative is,

$$\frac{\partial^2 k^{\mathrm{P}}(\boldsymbol{x}_i,\boldsymbol{x}_j)}{\partial \boldsymbol{x}_i \partial \boldsymbol{x}_j^{\mathrm{T}}}=\left[\frac{g(d_{ij})}{d_{ij}}-\frac{\partial g(d_{ij})}{\partial d_{ij}}\right]\boldsymbol{e}_{ij}\otimes\boldsymbol{e}_{ij}-\frac{g(d_{ij})}{d_{ij}}\cdot\mathbf{I} \tag{14}$$

Coordinate systems

Cartesian coordinates are known to be inefficient in geometry optimization[31,44,45] and are not suitable for large-sized local minimum search. Importantly, the Cartesian coordinates are not invariant with respect to the center-of-mass translation and overall rotation of the molecule. Curvilinear coordinates, on the other hand, represent the molecular structure with a non-linear combination of Cartesians, including a combination of bond length, valence angles, torsions, and out-of-plane improper torsions. These internal coordinates have been widely used in spectroscopy as well as first-principle geometry optimization. In our early work,[31] we implemented various curvilinear coordinates along with their gradient transformations in GPs, and in this work, we focus on the following three:

(1) The redundant internal coordinates,[46–48] $\boldsymbol{r}$, which contain more coordinates than the internal degrees of freedom (*i.e.*, $3N_{\mathrm{atm}} - 6$ for a non-linear molecule) and are generated by the transformation through Wilson's $\mathbf{B}$ matrix,[49] $\delta\boldsymbol{r} = \mathbf{B}\delta\boldsymbol{x}$, where $\delta\boldsymbol{x}$ is the displacements in atomic Cartesian coordinates.

(2) The non-redundant delocalized internal coordinates,[50] $\boldsymbol{s}$, which contain precisely $3N_{\mathrm{atm}} - 6$ coordinates for a non-linear molecule. They are constructed by combining the redundant internal coordinates *via* a linear transformation, $\boldsymbol{s} = \mathbf{U}^{\mathrm{T}}\boldsymbol{r}$, where $\mathbf{U}$ is the transformation, consisting of the set of non-redundant eigenvectors of $\mathbf{G} = \mathbf{B}^{\mathrm{T}}\mathbf{B}$ with positive eigenvalues.

(3) The Coulombic coordinates,[51,52] $\boldsymbol{C}$, which contain N_{atm} $(N_{\mathrm{atm}} - 1)/2$ unique interatomic distances. In particular, for a pair of atoms, i and j, $C_{ij} = 0.5Z_i^{2.4}$ when $i = j$, and $C_{ij} = Z_iZ_j/||\boldsymbol{R}_i - \boldsymbol{R}_j||$ when $i \neq j$, where Z_i is the nuclear charge of the atom i, and $||\boldsymbol{R}_i - \boldsymbol{R}_j||$ is the interatomic separation.

Overview of the physical prior GP optimization

In first-principle molecular geometry optimization, the overall cost is determined by the expense of evaluating QM forces and energy at each iteration, as well as the total number of iterations required to reach the local minimum (defined by the convergence threshold using the QM gradients). The cost of QM force and energy evaluation at an intermediate structure is intrinsically dictated by the electronic structure method and the size of the molecule (*i.e.*, the number of basis functions) and is therefore approximately invariant across iterations. Consequently, to evaluate the efficiency of the optimizer, our focus is on the number of iterations needed to achieve convergence, as the computational cost is proportional to this number.

The workflow of the physical prior-mean GP optimization algorithm is depicted in Scheme 1. We first start with an initial guess structure $\boldsymbol{x}_0$, and at the initial cycle, we call the QM solver (an electronic-structure method) to compute the energy and gradient at this point. If the gradient is lower than the convergence threshold, then the structure is converged. This is not the case in initial rounds, and one proceeds to include the current structure and its energy as well as the force in the on-the-fly GP training. In internal coordinate representation, we need to perform the coordinate transformation to transform the Cartesian-coordinate gradients ($\boldsymbol{g}_{\boldsymbol{x}}$) and Cartesian coordinates of the structure ($\boldsymbol{x}$) to the corresponding representation in the chosen internal coordinates ($\boldsymbol{g}_{\boldsymbol{q}}$ and $\boldsymbol{q}$). The details of this transformation in GP are reported in our prior work.[31] Next, we perform the GP training based on the training set at the current optimization iteration, which includes all intermediate structures generated so far (*i.e.*, $\boldsymbol{Q} = \{\boldsymbol{q}(\boldsymbol{x}_i)\}$). This training is based on the energy-and-force GP regression. We then search for a local minimum on the trained GP surrogate SPES, $E^{\mathrm{SPES}}(\boldsymbol{q})$, which will be converted back to the Cartesian-coordinate structural representation. This updated structure will be subject to a QM calculation to evaluate its energy and gradient, and if this

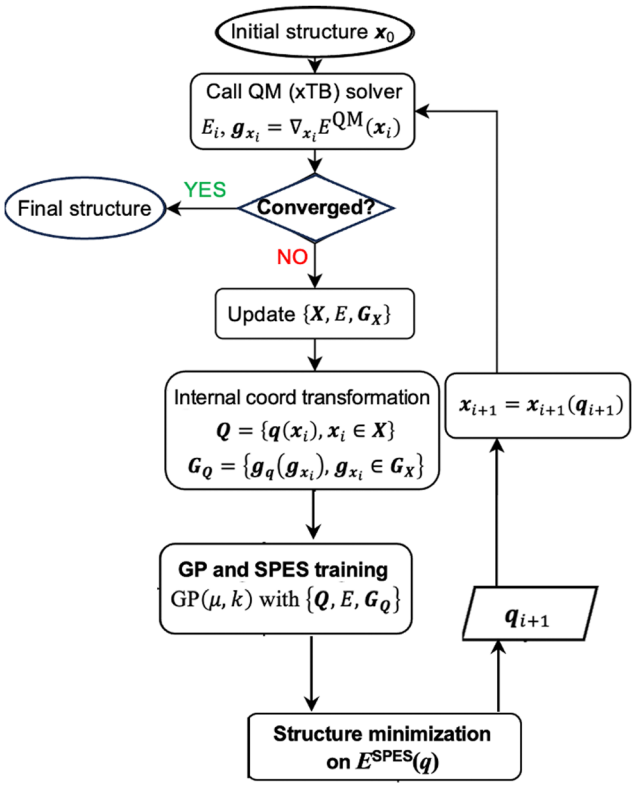

Scheme 1 Overview of the workflow of the physical prior-mean GP optimization algorithm.

structure is not a true local minimum at the QM level, the iteration continues. Each time we generate a new intermediate structure, the GP training set (denoted as the set $\{Q,E,G_Q\}$) is augmented to include its structure, QM energy, and QM gradient, and the GP SPES is updated based on the data accumulated.

III. Computational details

First-principle methods

All molecular structures are optimized to local minima quantum mechanically with the second-generation extended density-functional tight binding theory for geometries, vibrational frequencies, and non-covalent interactions (GFN2-xTB).[7] This is a quantitatively highly reliable and computationally efficient electronic structure theory suitable for large systems. The prediction error in bond lengths is less than 6 pm, and in non-covalent interactions, less than 3 kcal mol^{-1} (for main-group uncharged systems).[7] The target PESs in our physical GPs are thus the GFN2-xTB PESs. We utilize the implementation of GFN2-xTB in the xTB-python package (version 22.1).[53] In our physical GPs, the non-constant prior mean function used in this work is the semi-empirical Austin Model 1 (AM1) theory,[54] which is developed for quantitative descriptions of structures and energies around the local minima by introducing the modified neglect of differential overlap (MNDO) strategy in Hartree–Fock formalism with improved model parametrization. We implemented our GP optimizer to be interfaced with the Gaussian 16 C.01 program[55] for the evaluation of the AM1 electronic structure prior mean function.

Gaussian processes setting

The length scale hyperparameters in the kernel functionals are set to generic values. In particular, for the redundant internal and non-redundant delocalized internal coordinates, l = 1.8 bohr (~1 Å), in which an angle coordinate is converted to a unit of length by using the corresponding arc length in a circle of 1 bohr radius. For the Coulombic coordinates, l = 10 Å^{-1}, a generic value considering that the interatomic distance is on the order of 1 Å and the nuclear charge product is on the order of 10. The noise parameters $\sigma_e^2 = 4.0 \times 10^{-6}$ eV and $\sigma_f^2 = 2.5 \times 10^{-5}$ eV Å^{-1}. The structure search on the surrogate (SPES) is performed by energy minimization using the limited-memory Broyden–Fletcher–Goldfarb–Shanno with bounds (L-BFGS-B) optimizer, in which the bond-length internal coordinates are confined to be no less than 0.6 Å. The GP optimization is converged if the maximum Cartesian-coordinate force on an atom, evaluated by GFN2-xTB, is lower than f_{max}^{QM} = 0.05 eV Å^{-1}, a reasonable threshold for large-sized molecules (with more than 100 atoms). The surrogate structure minimization convergence threshold on the SPES is set to $0.05 f_{max}^{QM}$, in which f_{max}^{QM} corresponds to the latest geometry in the GP optimization.

Oligopeptide structure testing dataset

We have constructed a set of *de novo* oligopeptides to test the performance of using physical prior mean-driven GPs as a molecular structure optimizer in first-principle calculations. We have tabulated these 20 structures in the testing set in Table 1, detailing their components. Their initial geometries, the starting point for all the GP optimizer tests, are shown in

Table 1 The twenty constructed oligopeptides for GP optimizer performance test in this work

ID	Chemical formula	Secondary structure encoded	Amino acid sequence[a]
1	$C_{21}O_{11}N_{10}H_{34}$	Alpha helix	GGGAGGGGGG
2	$C_{27}O_{13}N_{11}S_2H_{45}$	Beta sheet	GAGCSGCGAGG
3	$C_{36}O_{17}N_{15}H_{59}$	Alpha helix	GPGEGGSAGR′GGS′
4	$C_{27}O_{12}N_9S_2H_{45}$	Alpha helix; cyclic	C′SSAAAAAC′
5	$C_{29}O_{16}N_{13}H_{47}$	Alpha helix	GSAGGGSGDGGG
6	$C_{26}O_{13}N_{14}H_{42}$	Beta sheet	GGGGGGGGGGGG′
7	$C_{31}O_{16}N_{13}SH_{47}$	Beta sheet	G′GCGNGGPGGGG
8	$C_{31}O_{16}N_{13}H_{47}$	Alpha helix	PGGDGGGGGGNG
9	$C_{38}O_{20}N_{18}H_{60}$	Beta sheet	GQGGGGGGSGGGGGGGG
10	$C_{32}O_{12}N_9S_2H_{43}$	Cyclic	G′GPC′NGGYC″
11	$C_{30}O_{16}N_{13}H_{47}$	Alpha helix	GGGGAGDGQGGG
12	$C_{32}O_{14}N_{11}H_{45}$	Linear	F′GEGGAGGGG′
13	$C_{33}O_{15}N_{12}S_2H_{48}$	Alpha helix; cyclic	C″GGPGGPGGGC′G
14	$C_{27}O_{15}N_{13}H_{43}$	Alpha helix	GGGGGGGGGGSG
15	$C_{33}O_{15}N_{15}H_{53}$	Beta sheet	GGGGGPGGGGGTGG′
16	$C_{29}O_{16}N_{13}H_{45}$	Beta sheet	GGANGDGGGGGG
17	$C_{34}O_{16}N_{15}S_4H_{51}$	Alpha helix; cyclic	C′GC′GGGGGGGC′GGGC′
18	$C_{36}O_{18}N_{17}H_{55}$	Beta sheet	G′GPGGGGGGGGGGGG″
19	$C_{35}O_{19}N_{17}H_{55}$	Alpha helix	GGGGGGGGGGGGGGSGG
20	$C_{38}O_{16}N_{18}H_{62}$	Beta sheet; cyclic	K′GGGGGGG′K′GGGGGGG′

[a] The amino acids are represented by their respective single-letter code. The code with a prime, *e.g.*, R′, indicates an artificial modification, as explained in the text.

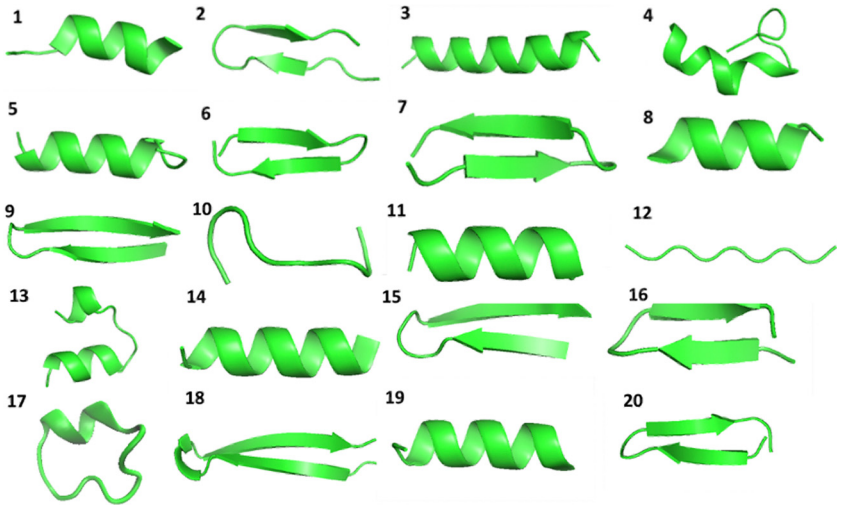

Fig. 1 The geometries of the 20 constructed oligopeptides in the testing set visualized using the ribbon model, in which the explicit atomistic arrangements are hidden. Notice that the heteroatoms are not represented in the ribbon model, so the cyclic oligopeptide structures 4, 10, 13, 17, and 20 are a bit obscured in atomic connectivity in this figure. The explicit all-atom ball-and-stick model of these structures is provided in the (ESI†).

Fig. 1 in ribbon diagrams, with all the atomic Cartesian coordinates (in Å) along with the full atomistic visualization provided in the ESI.† This set of test structures includes common amino acids and represents key secondary structures, such as the alpha helix, beta sheet, and cyclic structures (*e.g.*, the ones that are stabilized by disulfide bonds). We first selected a set of readily available protein structures and truncated them into oligopeptides to facilitate full QM-level structural optimization. The structures were then modified to ensure they function as true testing systems without any pre-training. Moreover, these oligopeptides do not occur naturally (to date), in which some of the amino acid side chains are mutated, making them well-suited for theoretical structural predictions and testing.

With the assistance of Gaussian16's built-in global MMX (GMMX) conformational search algorithm using the MMFF94 force field, one could pre-screen the peptide bond dihedral angles by searching within a subspace of the conformers (*e.g.*, limiting to 100 structures) stochastically and generate a reasonably low-energy initial structure. Nevertheless, for the purpose of this work, *i.e.*, testing the efficiency of the GP optimizers with various kernels and coordinates, we need not use the lowest-energy structures. In fact, it would be interesting to test if our method also works for higher energy structures (without any secondary structure). We created one such example (ID 12), for which its initial structure is linear.

In Table 1, the amino acid unit denoted with a prime, *e.g.*, R′, indicates an *ad hoc* modification performed on the natural structure. For ID 3, the side chain in R (arginine) is truncated to $-CH_2NH_2$, and in S (serine), its C-terminus has a $-CONH_2$ group instead of –COOH. For ID 4, both C's (cysteines) have their side chains forming a disulfide bridge (with a loss of H atoms), and the first C has its N-terminus defined as a –NHCOOH group, while the last C terminates the chain with an H atom instead of –COOH. For ID6, the G (glycine) has a $-CONH_2$ group as the C-terminus instead of –COOH. For ID7, the N-terminus in G starts with a –NHCOOH group instead of $-NH_2$. For ID10, the first G starts with a $-CONH_2$ group as its N-terminus, and the first C has its side chain forming a disulfide bridge, while the second C (*i.e.*, C″) loses the H atom on –SH in the side chain, and this chain ends with an H atom. For ID12, the first F (phenylalanine) starts with a –NHCOOH group at the N-terminus, and the G ends with a $-CONH_2$ group at the C-terminus. For ID13, the first C (*i.e.*, C″) starts with the –NHCOOH group at the N-terminus, and the –SH becomes a disulfide bridge, which is also the case for the second C. For ID15, the chain ends with a $-CONH_2$ group in G at the C-terminus. For ID17, all C's form the disulfide bridges. For ID18, the first G starts with a –NHCOOH group at the N-terminus, while the second G (*i.e.*, G″) ends with a $-CONH_2$ group at the C-terminus. For ID20, the side chain on K (lysine) connects with the C-terminus on G.

Structural comparison

We need to compare the structures predicted by GP optimizers, which differ in the kernel and coordinate representation, to ensure the same or similar structures were acquired. It is known that the optimized local minima may have slight discrepancies with different coordinate systems unless an extremely tight convergence threshold is applied. We define the reference structures as the QM-level local minima optimized with the non-redundant delocalized internal coordinates, $\boldsymbol{s}$, by the physical prior-mean GPs using the RQ kernel for IDs 2–5 and 7–20, the P kernel for ID 1, and the SE kernel for ID 6.

The root mean squared deviations (RMSDs in Å) in atomic Cartesian coordinates are calculated as a metric to assess the structural geometric differences. In particular, we used the Kabsch algorithm[56] in our comparison, in which the structures are re-centered and re-orientated to minimize the RMSD *via* the quaternions. In addition, we included the "--reorder" flag to perform the atom order adjustment to make sure that the order

of atoms (*i.e.*, atomic indices) in the two structures under comparison is consistent.

Furthermore, we have calculated the QM energy differences of the optimized local minima compared to the corresponding reference structures. We found that among all structures optimized by GPs when $\boldsymbol{r}$ and $\boldsymbol{s}$ coordinates were used, the energy differences were within 0.03 eV on average, and the RMSDs were within 0.2 Å on average. In the case of $\boldsymbol{C}$ coordinates, a few systems converged to higher energy conformers compared to the reference structures.

To show the limitation in the AlphaFold 3 prediction for oligopeptide structures, we also use RMSDs to compare our first-principle GP-optimized reference structures with the AlphaFold structures. Note that because our testing structures include modified amino acids and AlphaFold only takes in the natural amino acid sequence as input, we have to calculate the RMSDs for the common set of atoms shared by both predictions. In addition, if the atomic connectivity is different in two structures (physical GPs *vs.* AlphaFold), we exclude the case in our comparison.

IV. Results and discussions

We have tabulated the number of iterations for converging the 20 oligopeptides with the GP optimizers in Table 2, along with each optimizer's averaged number of iterations for reaching the local minima and the standard deviations. We have applied a combination of the kernel functionals (including the SE, RQ, M, and P kernels) and the structural descriptor (*i.e.*, the $\boldsymbol{r}$, $\boldsymbol{s}$, and $\boldsymbol{C}$ coordinates). The structural descriptor impacts the efficiency of the optimization significantly. In particular, the internal coordinates, including the $\boldsymbol{r}$ and $\boldsymbol{s}$, have a much better performance than the $\boldsymbol{C}$ coordinates. Although the $\boldsymbol{C}$ coordinates are indeed invariant with respect to the overall translation and rotation of the molecule, the inverse interatomic distance, $1/R_{ij}$, for a pair of well-separated nuclei is not sensitive to the structure change. In addition, the redundancy included in $\boldsymbol{C}$ is too high as compared to the other two coordinate systems. In particular, the number of unique coordinates scales as $\sim N_{\mathrm{atm}}{}^2$, which is unfavorable in such a high dimensional optimization task. Consequently, its performance in optimizing large-sized molecules, which have multiple large interatomic separations, is not optimal.

The synergistic effect of the kernel and coordinates is clear in our tests. In Fig. 2, we plot the average number of iterations, excluding the cases that failed to converge, in four kernel categories, each of which is subjected to three choices of the coordinate systems. The non-redundant delocalized internal coordinates, in general, show better performance than the other two coordinates for any kernel. For the Matern kernel, although $\boldsymbol{r}$ shows slightly better efficiency than $\boldsymbol{s}$ (199.8 *vs.* 218.5 iterations), since $\boldsymbol{s}$ only includes $3N_{\mathrm{atm}} - 6$ coordinates, it greatly reduces the memory requirement for GP optimizations.

One of the approaches to introduce a physically motivated learning model is through the design of the kernel in GPs. Our observation is consistent with the physical insights brought by the kernel. Specifically, the RQ and M kernels improve the modeling of the smoothness of realistic PESs as compared to the SE kernel, which is infinite-order differentiable. This is

Table 2 Number of iterations for structural convergence in GP optimizations (*i.e.*, the number of QM solver calls) with a combinatorial choice of kernel functionals (SE, RQ, M, and P) and coordinate systems ($\boldsymbol{x}$ = $\boldsymbol{r}$, $\boldsymbol{s}$, and $\boldsymbol{C}$) for the 20 oligopeptides in the testing set[a]

	$k^{\mathrm{SE}}(\boldsymbol{x}_i,\boldsymbol{x}_j)$			$k^{\mathrm{RQ}}(\boldsymbol{x}_i,\boldsymbol{x}_j)$			$k^{\mathrm{M}}(\boldsymbol{x}_i,\boldsymbol{x}_j)$			$k^{\mathrm{P}}(\boldsymbol{x}_i,\boldsymbol{x}_j)$		
ID	$\boldsymbol{r}$	$\boldsymbol{s}$	$\boldsymbol{C}$	$\boldsymbol{r}$	$\boldsymbol{s}$	$\boldsymbol{C}$	$\boldsymbol{r}$	$\boldsymbol{s}$	$\boldsymbol{C}$	$\boldsymbol{r}$	$\boldsymbol{s}$	$\boldsymbol{C}$
1	372	374	307	74	Failed	81	230	231	477	61	55	94
2	195	211	1308	43	42	580	130	130	1442	39	28	351
3	516	515	947	93	56	316	289	290	1623	72	67	305
4	210	206	1193	44	43	375	130	129	1435	43	43	512
5	250	261	807	49	53	127	151	150	743	65	67	172
6	55	59	471	Failed	Failed	103	26	27	455	Failed	Failed	101
7	159	168	441	25	34	62	93	95	368	33	33	151
8	608	738	824	116	111	130	351	344	838	120	101	172
9	123	123	487	28	24	67	79	78	478	26	25	118
10	96	92	874	26	20	136	24	24	887	19	18	160
11	281	279	667	50	48	98	154	152	590	58	53	136
12	65	59	264	13	13	130	14	14	156	12	9	39
13	111	109	1319	23	23	191	Failed	329	1320	24	23	222
14	625	566	807	105	99	126	308	315	701	60	75	349
15	436	Failed	895	91	55	139	281	211	783	88	95	287
16	157	157	739	32	30	114	91	91	661	34	30	88
17	1301	1235	Failed	189	180	Failed	Failed	695	Failed	Failed	Failed	731
18	391	Failed	582	60	72	94	256	252	586	76	65	236
19	761	753	925	129	126	197	535	544	780	93	86	143
20	439	390	739	97	71	123	455	269	985	Failed	Failed	222
Average	357.6	349.7	768.2	67.7	61.1	167.8	199.8	218.5	805.7	54.3	51.4	229.5
Std.	302.0	310.7	303.1	45.7	43.4	127.5	149.2	173.5	398.4	29.5	28.1	163.3

[a] The entry labeled "Failed" indicates that an unphysical structure is generated during the optimization process (*e.g.*, radical generation, broken bonds, *etc.*). For each column, the average number of iterations excludes any failed cases. The convergence threshold for all optimizers was set to the maximum atomic force (at QM level) being less than 0.05 eV Å^{-1}.

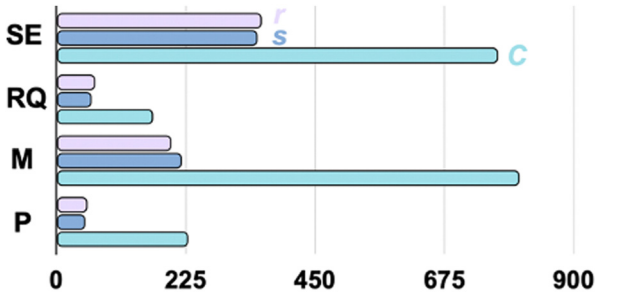

Fig. 2 The average number of iterations for converging the testing oligopeptides with the GP optimizers using the combinations of the kernel functionals (the squared exponential (SE), the rational quadratic (RQ), the twice-differentiable Matern (M), and the periodic (P) functionals) and the coordinate representations (the redundant internal (***r***, in violet), the non-redundant delocalized internal (***s***, in cerulean), and the Coulombic (***C***, in cyan) coordinates).

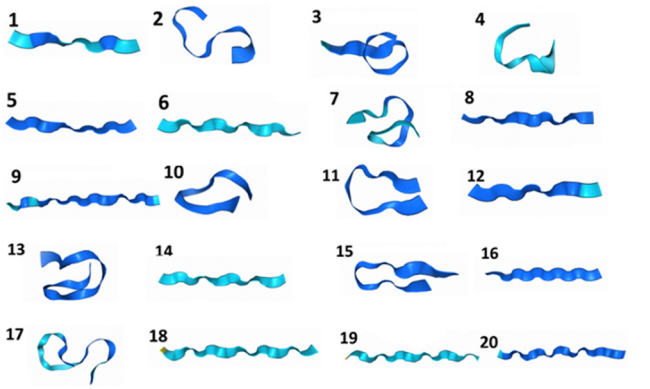

Fig. 3 The predicted oligopeptide structures generated by AlphaFold 3 in the ribbon model representation.

consistent with our performance test, in which the SE kernel is less efficient compared to the RQ and M kernels in general, except that $k^{SE}(\boldsymbol{C}_i,\boldsymbol{C}_j)$ is slightly more efficient than $k^{M}(\boldsymbol{C}_i,\boldsymbol{C}_j)$. When comparing the RQ with the M kernel, we found that the M kernel is less efficient, particularly when combined with the ***C*** coordinates. Nevertheless, when combined with ***s***, $k^{M}(\boldsymbol{s}_i,\boldsymbol{s}_j)$ is very robust because it successfully converged all 20 structures without convergence issues.

Overall, using $k^{P}(\boldsymbol{s}_i,\boldsymbol{s}_j)$ yields the best performance for our testing set, which, on average, only requires 51.4 iterations to reach convergence, which is a factor of $\sim$16 more efficient than $k^{M}(\boldsymbol{C}_i,\boldsymbol{C}_j)$. This observation shows the synergy between the periodic kernel and ***s***. The periodic kernel includes critical physical insights in optimizing oligopeptides or any molecule with a large number of internal rotations (torsional degree of freedom). When combined with internal coordinates, which include the dihedral angles for torsions, the local periodicity of the torsional motion, essential for geometry optimization in our task, generates a periodic function (the torsional projected PES). If one encounters a convergence failure with the $k^{P}(\boldsymbol{s}_i,\boldsymbol{s}_j)$-driven GP optimizer, an advisable solution without resorting to pre-optimize the structure with a classical force field is to switch to the RQ kernel in ***s*** coordinates, which provides similar performance.

Furthermore, under the periodic kernel, the redundant coordinate (***r***) requires 54.3 iterations on average, and thus, it performs similarly to the ***s*** coordinate system. Nevertheless, from the computational memory requirement perspective, the number of coordinates involved in the optimization for the non-redundant coordinate ***s*** is much fewer than the redundant coordinate choice ($>3N_{atm}$). Therefore, the ***s*** coordinate serves as a better choice than the ***r*** coordinates.

The final investigation we performed was to compare the first-principle structures optimized by the GP optimizer (in particular, the reference structure defined in the "Structural comparison" section) with the AlphaFold 3 predictions. These two approaches are fundamentally different in working principle, in which our physical GP method requires first-principle information and optimizes for local minima on the surrogate surfaces, while AlphaFold does not require detailed atomistic level energy calculations and aims for structural prediction for proteins. We have calculated the RMSDs in Å for all oligopeptides that have the same atomic connectivity predicted by these two models. Note that, in some cases (IDs 10 and 20), AlphaFold predicted completely different atomic connectivity compared to the first-principle optimized ones. The AlphaFold model uses the predicted template modeling (pTM) score to assess the prediction quality internally, indicating the overlap between the generated structure and the hypothetical true structure. All the predicted oligopeptides have a pTM score that falls within 0.02–0.03, drastically lower than the pTM = 0.5 threshold, indicating an internal diagnosis of highly unreliable predictions. The oligopeptide structures generated by AlphaFold tend to be linear and show no secondary structures (Fig. 3); thus, they are energetically unfavorable conformers compared to our GP-optimized ones at the QM level. The low pTM scores are consistent with our structural comparison in terms of the RMSDs, shown in Fig. 4, highlighting the

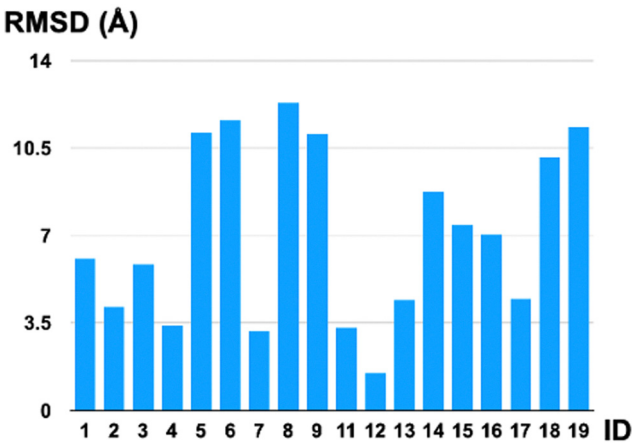

Fig. 4 The root mean squared deviations (RMSD in Å) comparison between the reference structures (QM-level GP optimized) and the AlphaFold 3 predicted structures (not first-principle-based) for the testing oligopeptides. Note that IDs 10 and 20 are excluded from this figure due to inconsistent atomic connectivity.

qualitatively different predictions from AlphaFold compared to the QM-level optimized structures. Even for the intentionally created linear structure, ID 12, for which our GP optimizer has no trouble optimizing to a local minimum quantum mechanically, the AlphaFold prediction still deviates from the reference by 1.5 Å. (Note that the C–H bond is ∼1.1 Å and the C–C bond is ∼1.5 Å.) The QM method, GFN2-xTB, is capable of predicting highly accurate geometries, with an error of ∼6 pm in bond lengths, and consequently, its local minima serve as benchmark-level structures in this work. This discrepancy is understandable since AlphaFold is trained on macromolecular complexes (proteins) without on-the-fly first-principle guidance in structural search. Furthermore, the smaller yet more flexible polypeptides are underrepresented in its training.

V. Conclusion

First-principle-level molecular structure optimization is an essential starting point for structure-based modeling and design. Large molecules with high degrees of freedom pose a challenge in the efficient search for local minima. We examined the usefulness of using a surrogate model-driven structure optimization for oligopeptides at the quantum mechanical level. In particular, we investigated the impact of the kernel functional choice and structural descriptor (including the redundant internal coordinates, the non-redundant delocalized internal coordinates, and the Coulombic coordinates) in physical prior mean-based GP optimizations. We concluded that for large torsionally flexible molecules, the periodic kernel, which approximates the physically periodic torsional potential energies, coupled with the delocalized internal coordinates, provides a highly efficient option for performing *ab initio* molecular geometry optimization with on-the-fly GP training and prediction.

Data availability

The data supporting this article have been included as part of the ESI.†

Conflicts of interest

There are no conflicts to declare.

Acknowledgements

J. L. B. acknowledges the financial support provided by the Schiller Institute Grant for Exploratory Collaborative Scholarship (SIGECS) as well as, in part, the American Chemical Society Petroleum Research Fund (PRF no. 65744-DNI6). In addition, we thank the Boston College Linux Cluster Center for cluster computing resources.

References

1 P. Hohenberg and W. Kohn, Inhomogeneous Electron Gas, *Phys. Rev.*, 1964, **136**, B864–B871.
2 W. Kohn and L. J. Sham, Self-Consistent Equations Including Exchange and Correlation Effects, *Phys. Rev.*, 1965, **140**, A1133–A1138.
3 D. Porezag, Th Frauenheim, Th Köhler, G. Seifert and R. Kaschner, Construction of Tight-Binding-Like Potentials on the Basis of Density-Functional Theory: Application to Carbon, *Phys. Rev. B: Condens. Matter Mater. Phys.*, 1995, **51**, 12947–12957.
4 M. Elstner, D. Porezag, G. Jungnickel, J. Elsner and M. Haugk, Th. Frauenheim, S. Suhai, and G. Seifert, Self-Consistent-Charge Density-Functional Tight-Binding Method for Simulations of Complex Materials Properties, *Phys. Rev. B: Condens. Matter Mater. Phys.*, 1998, **58**, 7260–7268.
5 M. Gaus, Q. Cui and M. Elstner, DFTB3: Extension of the Self-Consistent-Charge Density-Functional Tight-Binding Method (SCC-DFTB), *J. Chem. Theory Comput.*, 2011, **7**, 931–948.
6 A. S. Christensen, T. Kubař, Q. Cui and M. Elstner, Semiempirical Quantum Mechanical Methods for Noncovalent Interactions for Chemical and Biochemical Applications, *Chem. Rev.*, 2016, **116**, 5301–5337.
7 C. Bannwarth, S. Ehlert and S. Grimme, GFN2-*x*TB—An Accurate and Broadly Parametrized Self-Consistent Tight-Binding Quantum Chemical Method with Multipole Electrostatics and Density-Dependent Dispersion Contributions, *J. Chem. Theory Comput.*, 2019, **15**, 1652–1671.
8 M. Gaus, A. Goez and M. Elstner, Parametrization and Benchmark of DFTB3 for Organic Molecules, *J. Chem. Theory Comput.*, 2013, **9**, 338–354.
9 M. Gaus, X. Lu, M. Elstner and Q. Cui, Parameterization of DFTB3/3OB for Sulfur and Phosphorus for Chemical and Biological Applications, *J. Chem. Theory Comput.*, 2014, **10**, 1518–1537.
10 M. Gaus, H. Jin, D. Demapan, A. S. Christensen, P. Goyal, M. Elstner and Q. Cui, DFTB3 Parametrization for Copper: The Importance of Orbital Angular Momentum Dependence of Hubbard Parameters, *J. Chem. Theory Comput.*, 2015, **11**, 4205–4219.
11 S. Grimme, C. Bannwarth and P. Shushkov, A Robust and Accurate Tight-Binding Quantum Chemical Method for Structures, Vibrational Frequencies, and Noncovalent Interactions of Large Molecular Systems Parametrized for All spd-Block Elements (Z = 1–86), *J. Chem. Theory Comput.*, 2017, **13**, 1989–2009.
12 M. Vujovic, M. Huynh, S. Steiner, P. Garcia-Fernandez, M. Elstner, Q. Cui and M. Gruden, Exploring the Applicability of Density Functional Tight Binding to Transition Metal Ions. Parameterization for Nickel with the Spin-Polarized DFTB3 Model, *J. Comput. Chem.*, 2019, **40**, 400–413.
13 C. Bannwarth, E. Caldeweyher, S. Ehlert, A. Hansen, P. Pracht, J. Seibert, S. Spicher and S. Grimme, Extended

Tight-Binding Quantum Chemistry Methods, *Wiley Interdiscip. Rev.: Comput. Mol. Sci.*, 2021, **11**, e1493.

14 J. Jumper, R. Evans, A. Pritzel, T. Green, M. Figurnov, O. Ronneberger, K. Tunyasuvunakool, R. Bates, A. Žídek, A. Potapenko, A. Bridgland, C. Meyer, S. A. A. Kohl, A. J. Ballard, A. Cowie, B. Romera-Paredes, S. Nikolov, R. Jain, J. Adler, T. Back, S. Petersen, D. Reiman, E. Clancy, M. Zielinski, M. Steinegger, M. Pacholska, T. Berghammer, S. Bodenstein, D. Silver, O. Vinyals, A. W. Senior, K. Kavukcuoglu, P. Kohli and D. Hassabis, Highly Accurate Protein Structure Prediction with AlphaFold, *Nature*, 2021, **596**, 583–589.

15 M. Varadi, S. Anyango, M. Deshpande, S. Nair, C. Natassia, G. Yordanova, D. Yuan, O. Stroe, G. Wood, A. Laydon, A. Žídek, T. Green, K. Tunyasuvunakool, S. Petersen, J. Jumper, E. Clancy, R. Green, A. Vora, M. Lutfi, M. Figurnov, A. Cowie, N. Hobbs, P. Kohli, G. Kleywegt, E. Birney, D. Hassabis and S. Velankar, AlphaFold Protein Structure Database: Massively Expanding the Structural Coverage of Protein-Sequence Space with High-Accuracy Models, *Nucleic Acids Res.*, 2022, **50**, D439–D444.

16 M. Baek, F. DiMaio, I. Anishchenko, J. Dauparas, S. Ovchinnikov, G. R. Lee, J. Wang, Q. Cong, L. N. Kinch, R. D. Schaeffer, C. Millán, H. Park, C. Adams, C. R. Glassman, A. DeGiovanni, J. H. Pereira, A. V. Rodrigues, A. A. van Dijk, A. C. Ebrecht, D. J. Opperman, T. Sagmeister, C. Buhlheller, T. Pavkov-Keller, M. K. Rathinaswamy, U. Dalwadi, C. K. Yip, J. E. Burke, K. C. Garcia, N. V. Grishin, P. D. Adams, R. J. Read and D. Baker, Accurate Prediction of Protein Structures and Interactions Using a Three-Track Neural Network, *Science*, 2021, **373**, 871–876.

17 J. Abramson, J. Adler, J. Dunger, R. Evans, T. Green, A. Pritzel, O. Ronneberger, L. Willmore, A. J. Ballard, J. Bambrick, S. W. Bodenstein, D. A. Evans, C.-C. Hung, M. O'Neill, D. Reiman, K. Tunyasuvunakool, Z. Wu, A. Žemgulytė, E. Arvaniti, C. Beattie, O. Bertolli, A. Bridgland, A. Cherepanov, M. Congreve, A. I. Cowen-Rivers, A. Cowie, M. Figurnov, F. B. Fuchs, H. Gladman, R. Jain, Y. A. Khan, C. M. R. Low, K. Perlin, A. Potapenko, P. Savy, S. Singh, A. Stecula, A. Thillaisundaram, C. Tong, S. Yakneen, E. D. Zhong, M. Zielinski, A. Žídek, V. Bapst, P. Kohli, M. Jaderberg, D. Hassabis and J. M. Jumper, Accurate Structure Prediction of Biomolecular Interactions with AlphaFold 3, *Nature*, 2024, **630**, 493–500. (With the online server accessible *via* **https://alphafoldserver.com/about**; accessed on Nov. 12, 2024.).

18 K. Ahuja, W. H. Green and Y.-P. Li, Learning to Optimize Molecular Geometries Using Reinforcement Learning, *J. Chem. Theory Comput.*, 2021, **17**, 818–825.

19 C. Teng, Y. Wang, D. Huang, K. Martin, J.-B. Tristan and J. L. Bao, Dual-Level Training of Gaussian Processes with Physically Inspired Priors for Geometry Optimizations, *J. Chem. Theory Comput.*, 2022, **18**, 5739–5754.

20 A. Denzel and J. Kästner, Gaussian Process Regression for Geometry Optimization, *J. Chem. Phys.*, 2018, **148**, 094114.

21 D. Born and J. Kästner, Geometry Optimization in Internal Coordinates Based on Gaussian Process Regression: Comparison of Two Approaches, *J. Chem. Theory Comput.*, 2021, **17**, 5955–5967.

22 G. Raggi, I. Fdez Galván, C. L. Ritterhoff, M. Vacher and R. Lindh, Restricted-Variance Molecular Geometry Optimization Based on Gradient-Enhanced Kriging, *J. Chem. Theory Comput.*, 2020, **16**, 3989–4001.

23 I. F. Galván, G. Raggi and R. Lindh, Restricted-Variance Constrained, Reaction Path, and Transition State Molecular Optimizations Using Gradient-Enhanced Kriging, *J. Chem. Theory Comput.*, 2021, **17**, 571–582.

24 V. L. Deringer, A. P. Bartók, N. Bernstein, D. M. Wilkins, M. Ceriotti and G. Csányi, Gaussian Process Regression for Materials and Molecules, *Chem. Rev.*, 2021, **121**, 10073–10141.

25 R. Snyder, B. Kim, X. Pan, Y. Shao and J. Pu, Bridging Semiempirical and Ab Initio QM/MM Potentials by Gaussian Process Regression and Its Sparse Variants for Free Energy Simulation, *J. Chem. Phys.*, 2023, **159**, 054107.

26 J. Vandermause, S. B. Torrisi, S. Batzner, Y. Xie, L. Sun, A. M. Kolpak and B. Kozinsky, On-the-Fly Active Learning of Interpretable Bayesian Force Fields for Atomistic Rare Events, *npj Comput. Mater.*, 2020, **6**, 20.

27 B. Kolb, P. Marshall, B. Zhao, B. Jiang and H. Guo, Representing Global Reactive Potential Energy Surfaces Using Gaussian Processes, *J. Phys. Chem. A*, 2017, **121**, 2552–2557.

28 B. Jiang, J. Li and H. Guo, High-Fidelity Potential Energy Surfaces for Gas-Phase and Gas-Surface Scattering Processes from Machine Learning, *J. Phys. Chem. Lett.*, 2020, **11**, 5120–5131.

29 Y.-C. Chang and Y.-P. Li, Integrating Chemical Information into Reinforcement Learning for Enhanced Molecular Geometry Optimization, *J. Chem. Theory Comput.*, 2023, **19**, 8598–8609.

30 C. E. Rasmussen and C. K. I. Williams, *Gaussian Processes for Machine Learning*, MIT Press, 2006.

31 C. Teng, D. Huang and J. L. Bao, A Spur to Molecular Geometry Optimization: Gradient-Enhanced Universal Kriging with On-the-Fly Adaptive *Ab Initio* Prior Mean Functions in Curvilinear Coordinates, *J. Chem. Phys.*, 2023, **158**, 024112.

32 C. Teng, Y. Wang and J. L. Bao, Physical Prior Mean Function-Driven Gaussian Processes Search for Minimum-Energy Reaction Paths with a Climbing-Image Nudged Elastic Band: A General Method for Gas-Phase, Interfacial, and Bulk-Phase Reactions, *J. Chem. Theory Comput.*, 2024, **20**, 4308–4324.

33 C. Teng, D. Huang, E. Donahue and J. L. Bao, Exploring Torsional Conformer Space with Physical Prior Mean Function-Driven Meta-Gaussian Processes, *J. Chem. Phys.*, 2023, **159**, 214111.

34 M. G. Genton, Classes of Kernels for Machine Learning: A Statistics Perspective, *J. Mach. Learn. Res.*, 2001, **2**, 299–312.

35 S. Laue, M. Mitterreiter and J. Giesen, Computing Higher Order Derivatives of Matrix and Tensor Expressions, *Adv. Neural Inf. Process. Syst.*, 2018, **31**, 2750.

36 S. Laue, M. Mitterreiter and J. Giesen, A Simple and Efficient Tensor Calculus, *Proc. Assoc. Adv. Artif. Intell.*, 2020, **34**, 4527.

37 D. Huang, C. Teng, J. L. Bao and J.-B. Tristan, mad-GP: Automatic Differentiation of Gaussian Processes for Molecules and Materials, *J. Math. Chem.*, 2022, **60**, 969–1000.
38 M. L. Stein, *Interpolation of Spatial Data*, Springer-Verlag, New York, 1999.
39 J. Zheng, T. Yu, E. Papajak, I. M. Alecu, S. L. Mielke and D. G. Truhlar, Practical Methods for Including Torsional Anharmonicity in Thermochemical Calculations on Complex Molecules: The Internal-Coordinate Multi-Structural Approximation, *Phys. Chem. Chem. Phys.*, 2011, **13**, 10885–10907.
40 J. Zheng and D. G. Truhlar, Quantum Thermochemistry: Multistructural Method with Torsional Anharmonicity Based on a Coupled Torsional Potential, *J. Chem. Theory Comput.*, 2013, **9**, 1356–1367.
41 J. L. Bao, L. Xing and D. G. Truhlar, Dual-Level Method for Estimating Multistructural Partition Functions with Torsional Anharmonicity, *J. Chem. Theory Comput.*, 2017, **13**, 2511–2522.
42 L. Simon-Carballido, J. L. Bao, T. V. Alves, R. Meana-Pañeda, D. G. Truhlar and A. Fernandez-Ramos, Anharmonicity of Coupled Torsions: The Extended Two-Dimensional Torsion Method and Its Use to Assess More Approximate Methods, *J. Chem. Theory Comput.*, 2017, **13**, 3478–3492.
43 J. Zheng, S. L. Mielke, J. L. Bao, R. Meana-Pañeda, K. L. Clarkson and D. G. Truhlar, MSTor: A Program for Calculating Partition Functions, Free Energies, Enthalpies, Entropies, and Heat Capacities of Complex Molecules Including Torsional Anharmonicity, Version 2017-B, 2017.
44 H. B. Schlegel, Exploring Potential Energy Surfaces for Chemical Reactions: An Overview of Some Practical Methods, *J. Comput. Chem.*, 2003, **24**, 1514–1527.
45 M. von Arnim and R. Ahlrichs, Geometry Optimization in Generalized Natural Internal Coordinates, *J. Chem. Phys.*, 1999, **111**, 9183–9190.
46 G. Fogarasi, X. Zhou, P. W. Taylor and P. Pulay, The Calculation of Ab Initio Molecular Geometries: Efficient Optimization by Natural Internal Coordinates and Empirical Correction by Offset Forces, *J. Am. Chem. Soc.*, 1992, **114**, 8191–8201.
47 C. Peng, P. Y. Ayala, H. B. Schlegel and M. J. Frisch, Using Redundant Internal Coordinates to Optimize Equilibrium Geometries and Transition States, *J. Comput. Chem.*, 1996, **17**, 49–56.
48 V. Bakken and T. Helgaker, The Efficient Optimization of Molecular Geometries Using Redundant Internal Coordinates, *J. Chem. Phys.*, 2002, **117**, 9160–9174.
49 E. B. Wilson, J. C. Decius and P. C. Cross, *Molecular Vibrations: The Theory of Infrared and Raman Vibrational Spectra*, McGraw-Hill, 1955.
50 J. Baker, A. Kessi and B. Delley, The Generation and Use of Delocalized Internal Coordinates in Geometry Optimization, *J. Chem. Phys.*, 1996, **105**, 192–212.
51 M. Rupp, A. Tkatchenko, K. R. Müller and O. A. von Lilienfeld, Fast and Accurate Modeling of Molecular Atomization Energies with Machine Learning, *Phys. Rev. Lett.*, 2012, **108**, 058301.
52 F. Faber, A. Lindmaa, O. A. von Lilienfeld and R. Armiento, Crystal Structure Representations for Machine Learning Models of Formation Energies, *Int. J. Quantum Chem.*, 2015, **115**, 1094–1101.
53 Python API for the Extended Tight Binding Program. (With online access to the open-source code: **https://xtb-python.readthedocs.io/en/latest/**; accessed on Jan. 28, 2025.).
54 M. J. S. Dewar, E. G. Zoebisch, E. F. Healy and J. J. P. Stewart, AM1: A New General Purpose Quantum Mechanical Molecular Model, *J. Am. Chem. Soc.*, 1985, **107**, 3902–3909.
55 M. J. Frisch, G. W. Trucks, H. B. Schlegel, G. E. Scuseria, M. A. Robb, J. R. Cheeseman, G. Scalmani, V. Barone, G. A. Petersson, H. Nakatsuji, X. Li, M. Caricato, A. V. Marenich, J. Bloino, B. G. Janesko, R. Gomperts, B. Mennucci, H. P. Hratchian, J. V. Ortiz, A. F. Izmaylov, J. L. Sonnenberg, D. Williams-Young, F. Ding, F. Lipparini, F. Egidi, J. Goings, B. Peng, A. Petrone, T. Henderson, D. Ranasinghe, V. G. Zakrzewski, J. Gao, N. Rega, G. Zheng, W. Liang, M. Hada, M. Ehara, K. Toyota, R. Fukuda, J. Hasegawa, M. Ishida, T. Nakajima, Y. Honda, O. Kitao, H. Nakai, T. Vreven, K. Throssell, J. A. Montgomery Jr., J. E. Peralta, F. Ogliaro, M. J. Bearpark, J. J. Heyd, E. N. Brothers, K. N. Kudin, V. N. Staroverov, T. A. Keith, R. Kobayashi, J. Normand, K. Raghavachari, A. P. Rendell, J. C. Burant, S. S. Iyengar, J. Tomasi, M. Cossi, J. M. Millam, M. Klene, C. Adamo, R. Cammi, J. W. Ochterski, R. L. Martin, K. Morokuma, O. Farkas, J. B. Foresman and D. J. Fox, *Gaussian 16, Revision C.01.*, Gaussian, Inc., 2016.
56 K. W. Kabsch, A Solution for the Best Rotation to Relate Two Sets of Vectors, *Acta Crystallogr.*, 1976, **A32**, 922–923. (With online access to the open-source code: **https://github.com/charnley/rmsd**; accessed on Nov. 13, 2024.).